AIAA JOURNAL
Vol. 42, No. 10, October 2004

# Hypersonic Pressure, Skin-Friction, and Heat Transfer Distributions on Space Vehicles: Three-Dimensional Bodies

Amolak C. Jain*
*Science and Technology Corporation, Hampton, Virginia 23666*
and
James R. Hayes†
*U.S. Air Force Research Laboratory, Wright–Patterson Air Force Base, Ohio 45433*

**A new innovative engineering method is developed to predict surface quantity (pressure, skin-friction, and heat transfer) distributions on three-dimensional bodies, such as blunt-nosed bodies with circular and noncircular cross sections and bluff-nosed bodies of complex configuration. A key feature of the current procedure is to base three-dimensional effects on geometrical quantities associated with the three-dimensional body rather than the fluid mechanics of the flow on the three-dimensional body. The geometrical quantity is characteristic length associated with distinguishing features of the three-dimensional body. With the use of the stagnation Reynolds number with the characteristic length so defined in the analytical equations for each of the surface quantities, the surface quantities on three-dimensional bodies of simple and complex configurations are evaluated. The results from the engineering method on symmetrical and asymmetrical stagnation points, sphere–cones, elliptic paraboloids, and an aeroassist flight experiment vehicle, consisting of an ellipsoidal nose followed by an elliptic cone and a toroidal skirt, under hypersonic, rarefied and free molecular flow conditions agreed with available theoretical and experimental data with a reasonable accuracy. Wherever possible, emphasis is placed to provide a plausible explanation of three-dimensional fluid mechanical effects on the surface quantities of the given body.**

## Nomenclature

| | | |
|---|---|---|
| $a$ | = | semiminor axis of the elliptic paraboloid |
| $b$ | = | semimajor axis of the elliptic paraboloid |
| $C_f$ | = | skin-friction coefficient, $\tau_w/\frac{1}{2}\rho_\infty u_\infty^2$ |
| $C_{f0}$, $C_{f1}$ | = | coefficients defined in Eq. (2) |
| $C_h$ | = | heat transfer coefficient, $q_c/\frac{1}{2}\rho_\infty u_\infty^3$ |
| $C_{h0}$, $C_{h1}$ | = | coefficients defined in Eq. (3) |
| $C_{h3D}$ | = | heat transfer coefficient for a general, three-dimensional body defined in Eq. (4) |
| $C_{hsp}$ | = | heat transfer coefficient for a sphere |
| $C_p$ | = | pressure coefficient, $(p - p_\infty)/\frac{1}{2}\rho_\infty u_\infty^2$ |
| $C_{p0}$, $C_{p1}$, $C_{p2}$ | = | coefficients defined in Eq. (1) |
| $e$ | = | internal energy per unit mass |
| $H(x, y, z)$ | = | mean curvature at a point $(x, y, z)$ on a three-dimensional body |
| $H(0, 0, 0)$ | = | three-dimensional stagnation point mean curvature |
| $\tilde{H}(x, y, z)$ | = | mean curvature at a point $(x, y, z)$ on a three-dimensional body |
| $k$ | = | aspect ratio defined in Eq. (14) |
| $Kn$ | = | Knudsen number, $\lambda_\infty/L$ |
| $L$ | = | characteristic length |
| $M_\infty$ | = | freestream Mach number |
| $Pr$ | = | Prandtl number |
| $p$ | = | pressure per unit area |
| $q_c$ | = | heat flux per unit area |
| $Re_0$ | = | stagnation Reynolds number, $\rho_\infty u_\infty L/\mu(T_{e0})$ |
| $Re_{0sp}$ | = | stagnation Reynolds number of a sphere, $\rho_\infty u_\infty \rho_{yx}/\mu(T_{e0})$ |
| $Re_{01}$ | = | unit stagnation Reynolds number, $\rho_\infty u_\infty 1/\mu(T_{e0})$ |
| $r_n$ | = | nose radius of a spherical cone |
| $(r, \Phi, x)$ | = | cylindrical coordinates for aeroassist flight experiment vehicle shown in Fig. 15 |
| $(r, \Phi, z)$ | = | cylindrical coordinates for an elliptic paraboloid shown in Fig. 7 |
| $s$ | = | arc length measured from the stagnation point of a blunt body |
| $T$ | = | temperature |
| $T_{e0}$ | = | freestream stagnation temperature, $T_\infty\{1 + [(\gamma - 1)/2]M_\infty^2\}$ |
| $T_{wall}$ | = | wall temperature |
| $t$ | = | time, s |
| $t_{w0}$ | = | ratio of wall temperature to freestream temperature, $T_{wall}/T_{e0}$ |
| $u_\infty$ | = | freestream velocity |
| $(x, y, z)$ | = | Cartesian coordinates as shown in Figs. 7 and 15 |
| $\gamma$ | = | ratio of specific heats |
| $\theta$ | = | angle that the tangent at a point in the meridional plane $\Phi = \Phi^*$ of a three-dimensional body makes with the freestream |
| $\kappa_1$, $\kappa_2$ | = | stagnation point curvatures of a three-dimensional body along principal directions |
| $\lambda$ | = | defined in Eq. (18) |
| $\lambda_1$ | = | defined in Eq. (17) |
| $\lambda_\infty$ | = | mean free path in freestream |
| $\mu$ | = | viscosity coefficient |
| $\rho$ | = | density of the fluid |
| $\rho_{yx}$, $\rho_{yz}$ | = | radii of curvature at a point in a merdional plan $\Phi = \Phi^*$ of a three-dimensional body |
| $\tau_w$ | = | wall viscous shear stress |
| $\Phi$ | = | azimuthal angle of a meridional plane as shown in Figs. 7 and 15 |

Received 24 July 2003; revision received 2 June 2004; accepted for publication 2 June 2004. 

*Senior Research Scientist. Associate Fellow AIAA.
†Aerospace Engineer, Vehicle Integration Branch, AFRL/VAAA.

$\chi$ = ratio of principal curvatures at a point in a meridional plane $\Phi = \Phi^*$ of a three-dimensional body

*Subscripts and Superscripts*

$e0$ = freestream stagnation point
$\infty$ = freestream conditions
sp = defined for a sphere

## Introduction

IN Ref. 1, the capability of the new engineering method, called the Hypersonic Aerodynamic and Thermal Loads Analysis Program (HATLAP), to predict surface quantity (pressure coefficient $C_p$, skin-friction coefficient $C_f$, and heat transfer coefficient $C_h$) distributions on planar bodies is established with reasonable accuracy. Particular attention is paid to the unique capability of the HATLAP method to predict induced pressure due to viscous–inviscid interactions under hypersonic conditions and its effects on surface pressure, skin-friction, and heat transfer distributions on slender bodies. In this paper, the analytical procedure of Ref. 1 is extended to three-dimensional bodies such as blunt-nosed bodies with circular and noncircular cross sections and to bluff-nosed bodies of complex configuration with cross-sectional contours varying in shape and size. On a planar body such as a wedge, a fluid element near the surface suffers only longitudinal compression, whereas on a three-dimensional body such as a pointed cone, the surface fluid element suffers longitudinal as well as circumferential compression. As a result, the boundary layer becomes thin and the gradient of temperature near the wall increases, leading to an increase of heat wall fluxes on the cone in comparison to the heat fluxes on a wedge, whose semivertex angle is equal to the semivertex angle of the cone. Also, the shock is closer to the cone surface than on the wedge, and thus, the pressure is lesser on the cone than the pressure on the wedge. For axisymmetric bodies at zero angle of incidence, due to flow symmetry, circumferential expansion at each point in a cross section perpendicular to the axis of the body is the same. Hence, there is no crossflow velocity. Although the flow on the axisymmetric body is three-dimensional, due to zero crossflow velocity it is calculated from the two-dimensional form of the governing equations. For this reason, flows on axisymmetric bodies may be called two-dimensional. For asymmetric bodies with noncircular cross sections, circumferential expansion differs from point to point across a cross section perpendicular to the body axis, giving rise to crossflow velocity. The crossflow velocity magnitude depends on the mean curvature at points across the cross section. The mean curvature at a point on the three-dimensional body is defined as the mean of principal curvatures along the principal directions, that is, the directions in which the maximum and minimum curvatures lie at the point on the body. A full mathematical description of the analytical expression for the mean curvature is given by Weatherburn.[2] Tirskii et al.[3] also derived an expression for the mean curvature in a nonorthogonal curvilinear coordinate system. Crossflow velocity leads to the spreading of streamlines in transverse direction. Crossflow velocity draws mass, momentum, and energy transverse to the longitudinal direction and changes the heat fluxes in comparison to the heat fluxes on an equivalent axisymmetric body. An equivalent axisymmetric body (EAB) is formed by rotating the generatrix in the given meridional plane, about the axis of the three-dimensinal body. A rigorous definition of the EAB is given later in the text.

On a bluff-nosed body with cross-sectional contour varying in shape and size with axial distances, heat fluxes depend on the equivalent axisymmetric effects or axisymmetric effects in simple terms and bluntness effects. Axisymmetric effects bring the shock nearer to the surface and increase heat fluxes, whereas bluntness effects tend to push the shock farther away and decrease the heat fluxes. On a general three-dimensional blunt body, axisymmetric effects may dominate the bluntness effects on some portion of the body and, thus, increase the heat fluxes, whereas the opposite may happen on another part of the body. In view of the opposing effects on heat transfer from the axisymmetric and the blunt components of the bluff body, it may be difficult to make a general statement about the effect of three-dimensionality on heat fluxes on a general three-dimensional bluff-nosed body of complex configuration.

Jain and Hayes[1] discussed in detail that the aeroheating,[4] the INCHES,[5] and the MINIVER[6] (miniature version of the JA70 aerodynamic heating computer program, H800[7]) codes have limited capability to predict heat fluxes on a three-dimensional body. The MINIVER[6] code uses the Mangler transformation to derive heat fluxes on conical bodies with no pressure gradient and Prandtl number equal to unity, from that of a flat plate. Application of this approach to a general three-dimensional body with pressure gradient and Prandtl number different from unity will incur significant error. Cooke's analogy[8] forms the basis of the aeroheating[4] and the INCHES[5] codes generally to derive heat fluxes on a three-dimensional body from an axisymmetric body and is based upon the assumption of small cross-flow velocity with respect to the free stream velocity. A full discussion of the basis assumptions of Cooke analogy[8] and its applications to three-dimensional bodies is given by Jain and Hayes.[1] Besides the technical difficulties associated with the calculation of inviscid streamline divergence outside the boundary layers and the associated metric coefficient, the method gives results on or near the symmetry planes of the body. In the present approach, three-dimensional effects on heat fluxes are based on geometrical quantities associated with the three-dimensional body rather than the fluid mechanics of the three-dimensional body. Geometrical quantities need be calculated only once. Then, the HATLAP method can predict surface quantities at all points of a given trajectory. This procedure based on geometrical quantities, besides being simpler to use in comparison to the ones based on calculating the gasdynamics at each point of the trajectory, has a much wider range of applicability because it envisages no restrictions on crossflow velocity. It is applicable to all meridional planes of a given three-dimensional body before separation occurs. Also, the present procedure, besides providing information on thermal load distributions, provides aerodynamics (surface pressure and skin-friction) results for general three-dimensional configurations.

Validity of the approach is established by comparing the results from the present approach on axisymmetric bodies such as sphere–cones, asymmetric bodies such as elliptic paraboloids, and three-dimensional bluff-nosed bodies of complex configuration such as an Aeroassist Flight Experiment (AFE) vehicle, with the well-established computational fluid dynamics (CFD), direct simulation of Monte Carlo (DSMC), and wind-tunnel and flight data under flight conditions ranging from hypersonic continuum to free molecular regimes. In all cases, the agreement is found to be good to excellent.

## Description of Method

The algebraic equations describing pressure, skin-friction and heat transfer coefficient distributions are the following:

$$C_p = C_{p0} + C_{p1} \times \sin\theta + C_{p2} \times \sin^2\theta \tag{1}$$

$$C_f = C_{f0} \times \cos\theta + C_{f1} \times \sin\theta \times \cos\theta \tag{2}$$

$$C_h = C_{h0} + C_{h1} \times \sin\theta \tag{3}$$

The coefficients $C_{pi}$, $i = 0, 1, 2$, $C_{fi}$, $i = 0, 1$, and $C_{hi}$, $i = 0, 1$, are functions of freestream Mach number $M_\infty$, stagnation Reynolds number $Re_0$, ratio of specific heats $\gamma$, ratio of wall temperature to stagnation temperature $t_{w0}$, and Prandtl number $Pr$. A brief description of the coefficients in Eqs. (1–3) is given by Jain and Hayes.[1] Full mathematical expressions for the coefficients in Eqs. (1–3) are given by Jain.[9]

Equations (1–3) are applied to determine aerodynamic and thermal load distributions on bodies of revolution with circular and noncircular cross sections and to three-dimensional bluff-nosed bodies of complex configuration. For each body type, only the description of the characteristic length used in defining the stagnation Reynolds number changes. For sharp-edged flat plates or wedges, the characteristic length is the running length from the tip of the plate or

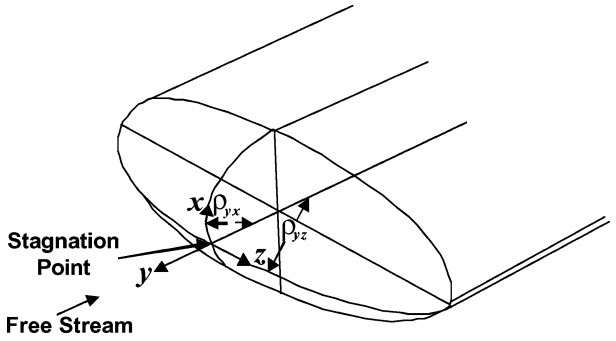


**Fig. 1 Coordinate system for a general three-dimensional stagnation point.[10]**

wedge. For spheres, the characteristic length is the radius of the sphere. For sphere–cones, the characteristic length for the spherical portion is the sphere radius and that for the conical portion is the running length from the stagnation point of the spherical nose. For blunt-nosed asymmetrical bodies, the stagnation point characteristic length is determined by the following procedure introduced by Reshotko[10] and is presently modified to extend its applicability to the three-dimensional body downstream the three-dimensional stagnation point.

By using a series of transformations and approximations, Reshotko[10] reduced the three-dimensional compressible, similar boundary-layer equations for a triaxial stagnation point (Fig. 1) to the two-dimensional boundary-layer equations for the stagnation point of a sphere with an effective nose radius. He correlated the three-dimensional stagnation point heat transfer coefficient $C_{h3D}$ of a triaxial ellipsoid with the heat transfer coefficient $C_{hsp}$ of a two-dimensional stagnation point of a sphere by the following relation:

$$C_{h3D} = \sqrt{(1+\chi)/2} \times C_{hsp}\left(Re_{0sp}\right) \tag{4}$$

where

$$\chi = \frac{\rho_{yx}}{\rho_{yz}}, \qquad \rho_{yx} < \rho_{yz}$$

$$Re_{0sp} = \frac{\rho_\infty u_\infty \rho_{yx}}{\mu(T_{e0})}$$

From Fay and Riddell,[11]

$$C_{hsp}(Re_{0sp}) \propto 1\Big/\sqrt{Re_{0sp}} \tag{5}$$

Equation (4) can be written as

$$C_{h3D} \propto \sqrt{(1+\chi)/2} \times \sqrt{1/Re_{0sp}}$$

$$= \sqrt{\tfrac{1}{2}(1/\rho_{yx} + 1/\rho_{yz}) \times \mu(T_{e0})/\rho_\infty u_\infty 1} \tag{6}$$

$$C_{h3D} \propto \sqrt{(1+\chi)/2} \times \sqrt{1/Re_{0sp}} = \sqrt{(\kappa_1+\kappa_2)/2 \times 1/Re_{01}} \tag{7}$$

where $Re_{01} = \rho_\infty u_\infty 1/\mu(T_{e0})$ is the unit stagnation Reynolds number and $\kappa_1$ and $\kappa_2$ are stagnation point curvatures along the $yx$ and $yz$ axis, respectively,

$$C_{h3D} \propto \sqrt{H(0,0,0)/Re_{01}} \tag{8}$$

Let

$$Re_0 = 1/H(0,0,0) \times Re_{01} \tag{9}$$

From Eqs. (4–9),

$$C_{h3D} = C_{hsp}(Re_0) \tag{10}$$

Since

$$Re_0 > Re_{0sp}, \qquad C_{h3D} = C_{hsp}(Re_0) < C_{hsp}(Re_{0sp}) \tag{11}$$

Equations (11) correlate the three-dimensional triaxial stagnation point heat transfer coefficient with the spherical stagnation point heat transfer coefficient provided the radius of the sphere is given by $[1/H(0,0,0)]$. For the case of a cylinder held perpendicular to the freestream flow, then, from Eq. (7),

$$\kappa_2 = 0.0, \qquad Re_0 = 2.0 \times Re_{0sp} \tag{12}$$

The heat transfer coefficient along the stagnation line of the cylinder is

$$(C_{h3D})_{\text{cylinder}} = 1\Big/\sqrt{2} C_{hsp}(Re_{0sp})$$

This is the same result as obtained by Lees.[12]

For a three-dimensional general stagnation point heat transfer coefficient, it is easy to use Eqs. (1–3) with stagnation Reynolds number defined with the characteristic length,

$$L = 1/H(0,0,0) \tag{13}$$

and $\theta = 90$ deg to determine the three-dimensinal stagnation point pressure, skin-friction, and heat transfer coefficients, respectively. The three-dimensional effects are incorporated in the definition of the characteristic length. This approach enables us to determine not only the three-dimensional stagnation point values of $C_p$, $C_f$, and $C_h$, but also helps us to generalize its application to points on the three-dimensional body downstream of the three-dimensional stagnation point. Although the current method can determine $C_p$ and $C_f$, the emphasis in this paper is placed on calculating $C_h$ on three-dimensional bodies.

Further generalization of the described approach can be made by considering the characteristic length

$$L = 1/H(x, y, z) \tag{14}$$

where $H(x, y, z)$ is the mean curvature at the point $(x, y, z)$ on the three-dimensional body lying on a meridional plane inclined at an angle $\Phi = \Phi^*$ with the $yz$ plane (Fig. 1),

$$Re_0 = 1/H(x, y, z) \times Re_{01} \tag{15}$$

If $\theta$ is defined as the angle that a tangent at a point in the meridional plane $\Phi = \Phi^*$ on the three-dimensional body makes with the freestream, Eqs. (1–3) with $Re_0$ given by Eq. (15) give the pressure coefficient $C_p$, skin-friction coefficient $C_f$, and heat transfer distribution $C_h$ along the meridional plane $\Phi = \Phi^*$ of the three-dimensional body.

To represent the effect of actual pressure distribution on the three-dimensional body departing from the one predicted by the Newtonian pressure, Tirskii et al.[3] modified the definition of the characteristic length as follows:

$$L = \lambda_1/H(x, y, z) \tag{16}$$

where

$$\lambda_1 = 1.0 + \frac{4}{15} \times \frac{f_{xx} f_x^2 + 2 f_{xy} f_x f_y + f_{yy} f_y^2}{\left(1 + f_x^2 + f_y^2\right)^{\frac{3}{4}} \times H(x, y, z)} \tag{17}$$

where $z = f(x, y)$ is the equation of the three-dimensional body and $f_x$, $f_y$, $f_{xy}$, $f_{xx}$, and $f_{yy}$ are the derivatives of $f(x, y)$ with respect to the subscripts.

For a bluff body with a complex configuration and having cross-sectional contours with varying shape and size, there are opposite effects of axisymmetry and bluntness. Based on a large number of numerical and analytical solutions of two-dimensional and three-dimensional viscous shock layer (VSL) equations with surface slip and shock slip boundary conditions, Tirskii et al.[3] derived the following rule to derive the definition of the characteristic length.

Tirskii et al.[3] envisaged an EAB whose angle $\tilde{\alpha}$, the angle that the normal at any point to the generatrix makes with the freestream, is equal to the angle $\alpha$, the angle that the normal at the point on the given three-dimensional body makes with the freestream. If the mean curvature at any point $(x, y, z)$ of the generatrix of the EAB is given by $\tilde{H}(x, y, z)$, then the characteristic length at the point $(x, y, z)$ on the generatrix of a general three-dimensional body is given by the following:

$$L = \tilde{H}(x, y, z)/H(x, y, z) \times \lambda/\tilde{H}(0, 0, 0) \tag{18}$$

Golovachov[13] defined the value of $\lambda$ as follows:

$$\lambda = 1.0 + \frac{4}{15} \times \frac{f_{xx} f_x^2 + 2 f_{xy} f_x f_y + f_{yy} f_y^2}{\left(1 + f_x^2 + f_y^2\right)^{\frac{3}{2}} \times H(x, y, z)} \tag{19}$$

where $z = f(x, y)$ is the equation of the three-dimensional body under consideration and

$$Re_0 = L \times Re_{01} \tag{20}$$

Values of $\tilde{H}(x, y, z)$ and $H(x, y, z)$ are given by Tirskii et al.[3] and are so reported by Jain.[9] Tirskii et al.[3] used the definition of stagnation Reynolds number given by Eq. (20) to solve two-dimensional VSL equations for axisymmetric flows to predict heat flux distributions on two-dimensional bodies. The process of solving the two-dimensional VSL equations on a body of complex configuration is quite tedious and time consuming. As such, this procedure has not been adopted here because it does not fall in the category of engineering procedure.

In the present investigation, the stagnation Reynolds number defined by Eq. (20) is used in Eqs. (1–3) to give pressure, skin-friction, and heat transfer coefficient distributions in the meridional planes of the three-dimensional bluff body of complex configuration such as an AFE vehicle. Once the values of $\lambda$, $\tilde{H}$, and $H$ are calculated, the process of evaluating $C_p$, $C_f$, and $C_h$ from algebraic equations (1–3) become simple enough for engineering use. The mathematical procedure of deriving analytical expressions for the EAB, $\lambda(x, y, z)$, $\tilde{H}(x, y, z)$, and $H(x, y, z)$ for a body of general shape is described by Tirskii et al.[3] and by Jain.[9] The analytical expressions for $\lambda_1$ and $H(x, y, z)$ for elliptic paraboloids are derived by Jain,[14] and the expressions for $\lambda(x, y, z)$, $\tilde{H}(x, y, z)$, and $H(x, y, z)$ for the AFE vehicle are presented by Jain.[15]

## Discussion of Results

### Shuttle Stagnation Point

Moss and Bird[16] made DSMC calculations for heat transfer coefficient $C_h$ at the stagnation point of the Space Shuttle Orbiter nose flying at altitudes from 92.25 to 150 km with nonequilibrium chemical reactions and compared the results with VSL solutions without slip boundary conditions. The results indicated that the chemical reactions within the flowfield are evident up to the altitude of about 105 km, and beyond 105 km, the gas composition in the shock layer is basically the same as that of the freestream.

Under the shuttle flight conditions given by Moss and Bird,[16] the present results for heat transfer coefficient $C_h$ at the stagnation point of the Space Shuttle Orbiter nose have been obtained from Eq. (3) for a perfect gas with effective $\gamma$. An effective $\gamma$ is defined as the $\gamma$ of a mixture of inert gases present in the freestream. Also, continuum stagnation point results for $C_h$ are calculated from the Fay and Riddell[11] formula. In Fig. 2, the present results of $C_h$ from Eq. (3) are compared with the DSMC result of Moss and Bird[16] and the continuum results of Fay and Riddell.[11] Figure 2 indicates that at the lowest altitude of the trajectory, namely, 92.25 km ($Kn = 0.028$), the present results differ from the DSMC results by less than 8%, indicating a mild effect of nonequilibrium chemistry on $C_h$. At the next trajectory point of 99.49 km, the percentage difference is 1.17%. Beyond 99.49 km, the differences between the present results and the DSMC results are less than 5%. It is surprising to note that the continuum results of Fay and Riddell[11] agree with the present results and the DSMC results up to 104.49 km ($Kn = 0.227$) within

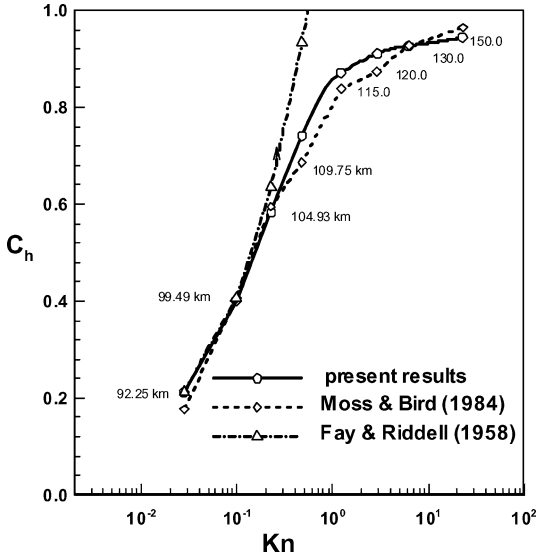


**Fig. 2 Comparisons of the present results at the Space Shuttle Orbiter stagnation point with Moss and Bird[16] and Fay and Riddell[11] results.**

a difference of 9%. This observation extends the range of applicability of the Fay and Riddell[9] formula into the rarefied regime. Beyond 104.49 km, Fay and Riddell[9] results continue to attain substantially higher values of $C_h$ in comparison with both the present and the DSMC results, indicating the failure of the Fay and Riddell[11] formulation.

### Fire II Capsule Stagnation Point

To provide benchmark data for CFD code validation, NASA injected the Fire II reentry capsule into the atmosphere at an altitude of 121.24 km with a velocity of 11.35 km/s. The Fire II capsule consisted of three beryllium calorimeters separated by asbestos sheets with an effective nose radius of 0.747, 0.656, and 0.600 m, respectively. Freestream conditions for each phase of recording data is given in Table 1. Gupta[17] calculated the stagnation point convective and radiative heat fluxes using a two-dimensional VSL code with equilibrium chemistry and coupled it with the aerotherm radiation code, RAD.[18] Gupta[17] also solved the Navier–Stokes (NS) equations with slip conditions and nonequilibrium chemistry for a few high-altitude points of the reentry trajectory. Balakrishnan[19] determined the stagnation point heating using inverse procedure based upon the VSL equations with equilibrium chemistry, coupled with the radiative code called RASLE developed by Nicolet and Balakrishnan.[20] Present calculations with the HATLAP method have been performed with perfect and equilibrium gas conditions and reported by Jain[21] and with radiative heating using the engineering relation by Neuenschwander[22] for the three phases of the reentry trajectory.

In view of wide differences in radiative heating from the three mentioned approaches, it was considered desirable not to include the radiative component of heating in the total heating. This exclusion will enable us to have a fair assessment of the capability of the HATLAP code. In Table 1, flight conditions in the various phases, convective heatings from Gupta,[17] Balakrishnan,[19] and the HATLAP code for perfect and equilibrium cases[21] are presented for comparison purposes. In Table 1, it can be seen that the equilibrium values from Gupta[17] and Balakrishnan[19] computations are almost the same. It really does not matter which results are chosen for comparison purposes. In the present investigation, percentage differences of our results are calculated with Gupta[17] results.

Results from the NS equations at time $t = 1632$, 1634, and 1640.5 s differ from the corresponding VSL results of Gupta[17] by 28.45, 17.27, and 12.16%, respectively. Jain and Prabha[23] have shown that the departure of the NS equation results from the VSL results takes place due to the predominance of rarefaction effects. Moss and

**Table 1 Comparison of convective stagnation point heat fluxes for the Fire II vehicle flight condition**

| Effective nose radius $R_N$, m | Time, s | Altitude, km | Velocity, km/s | $\dot{q}_c$, W/cm$^2$ Equilibrium, Gupta[17] | Equilibrium, Balakrishnan[19] | Perfect gas with effective gamma, HATLAP | Equilibrium, HATLAP | Percentage difference in $\dot{q}_c$ between HATLAP Gupta's equilibrium results[a] | $Kn$ |
|---|---|---|---|---|---|---|---|---|---|
| | | | | | *Heat shield 1* | | | | |
| 0.747 | 1631.0 | 84.60 | 11.37 | 105.3 | 111.9 | 100.61 | | +5.26 | 0.0083 |
| 0.747 | 1632.0 | 81.86 | 11.37 | 134.6 (172.9)[b] | 135.0 | 125.37 | | +7.36 | 0.0053 |
| 0.747 | 1634.0 | 76.42 | 11.36 | 208.5 (172.5)[b] | 203.0 | 199.86 | | +4.32 | 0.0020 |
| 0.747 | 1636.0 | 71.04 | 11.31 | 287.8 (252.1)[b] | 292.8 | 295.39 | | −2.57 | 0.00088 |
| 0.747 | 1637.5 | 67.05 | 11.25 | 350.7 | 341.6 | 375.72 | | −7.32 | 0.00053 |
| 0.747 | 1639.0 | 63.11 | 11.14 | 442.0 | 450.6 | 459.57 | | −3.98 | 0.00033 |
| 0.747 | 1640.5 | 59.23 | 10.97 | 543.0 (540.3)[b] | 509.6 | 548.28 | | −0.97 | 0.00021 |
| 0.747 | 1642.0 | 55.48 | 10.71 | 610.5 | 608.3 | 632.96 | | −3.68 | $0.134\times10^{-3}$ |
| | | | | | *Heat shield 2* | | | | |
| 0.656 | 1642.7 | 53.77 | 10.55 | 684.7 | 653.7 | 754.57 | 697.59 | −1.85 | $0.128\times10^{-3}$ |
| 0.656 | 1643.0 | 53.04 | 10.48 | 705.3 | 687.8 | 759.43 | 706.40 | −0.16 | $0.118\times10^{-3}$ |
| 0.656 | 1644.0 | 50.67 | 10.19 | 741.9 | 708.2 | 772.55 | 732.28 | +1.31 | $0.910\times10^{-4}$ |
| 0.656 | 1645.0 | 48.37 | 9.83 | 757.1 | 712.7 | 775.76 | 743.41 | +1.84 | $0.705\times10^{-4}$ |
| 0.656 | 1646.5 | 45.14 | 9.16 | 755.6 | 696.8 | 759.81 | 726.58 | +3.99 | $0.466\times10^{-4}$ |
| 0.656 | 1648.0 | 42.14 | 8.30 | 669.2 | 590.1 | 681.60 | 645.72 | +3.64 | $0.305\times10^{-4}$ |
| | | | | | *Heat shield 3* | | | | |
| 0.600 | 1648.3 | 41.60 | 8.10 | 696.0 | 625.0 | 743.53 | 694.15 | +0.27 | $0.307\times10^{-4}$ |
| 0.600 | 1649.5 | 39.50 | 7.27 | 566.1 | 539.0 | 599.06 | 561.34 | +0.85 | $0.224\times10^{-4}$ |
| 0.600 | 1651.0 | 37.19 | 6.19 | 433.5 | | 411.63 | 388.11 | +11.70 | $0.163\times10^{-4}$ |
| 0.600 | 1652.0 | 35.86 | 5.49 | 327.5 | | 304.00 | 288.73 | +13.43 | $0.136\times10^{-4}$ |
| 0.600 | 1653.0 | 34.88 | 4.85 | 238.8 | | 220.23 | 209.19 | +14.18 | $0.113\times10^{-4}$ |

[a]Percentage of difference $= (\dot{q}_c)_{\text{Gupta, VSL equil}} - (\dot{q}_c)_{\text{HATLAP}}/(\dot{q}_c)_{\text{HATLAP}} \times 100$. [b]Results from the NS code with nonequilibrium chemistry.

Bird[16] pointed out that under highly rarefied conditions, chemical reactions cease and composition of the gas in the shock layer is the same as in the ambient gas. As such, it is considered appropriate to compare the results from the HATLAP code with perfect gas[21] with Gupta's equilibrium gas results during phase 1 of the flight. Table 1 shows that, except for the last three points toward the end of the phase 3 portion of the reentry trajectory, the percentage difference between the current HATLAP equilibrium gas[21] and that of Gupta's[17] equilibrium gas results is less than 8%. The percentage difference at the last three points of the trajectory, namely, at time $t = 1651$, 1652, and 1653 s is less than 15%. Note that for some reasons, Balakrishnan[19] did not compute the results of $C_h$ at times $t = 1651$, 1652, and 1653 s. Under the circumstances, it is difficult to attribute any reason for the large difference in the values of $C_h$ from the HATLAP and Gupta[17] results at the last three points of the Fire II trajectory. In Fig. 3, results from the cited approaches are drawn to show the success of the HATLAP method to predict heating with reasonable accuracy in the harsh environment of the Fire II trajectory.

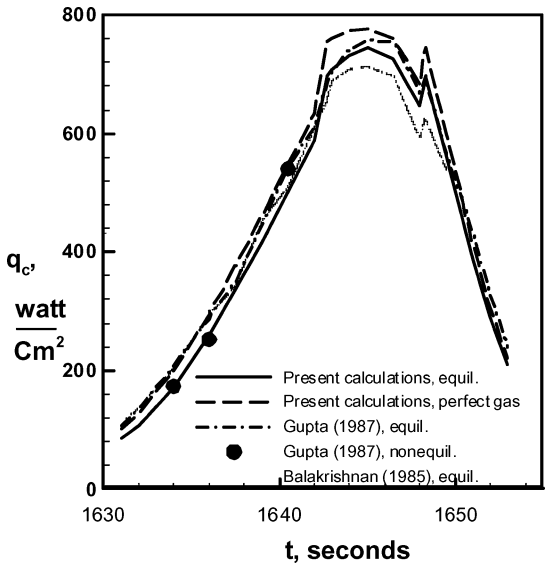


**Fig. 3 Comparisons of the present results at the Fire II capsule stagnation point with Gupta[17] and Balakrishnan[19] results.**

### Sphere–Cones

Moss et al.[24] provided DSMC calculations of $C_h$ with chemical nonequilibrium effects on a 5-deg sphere–cone of nose radius 0.0254 m with a wall temperature of 1000 K and with a constant velocity of 7.5 km/s at altitudes of 70 ($Kn = 0.032$), 80 ($Kn = 0.156$), and 100 km ($Kn = 5.384$). In the present investigation, the results of $C_h$ from Eq. (3) of the HATLAP code with perfect gas have been carried out under the same prescribed conditions as given by Moss et al.[24] The characteristic length used in the definition of the stagnation Reynolds number in Eq. (3) is taken as nose radius for the spherical portion and the characteristic length for the conical portion is defined in three different ways: 1) circular base radius of the conical frustum, 2) circular base diameter of the conical frustum, and 3) running length from the stagnation point of the spherical nose. Comparison of the $C_h$ results against the arc length $s$, measured from the stagnation point of the 5-deg sphere–cone, from each of the mentioned options with the corresponding DSMC results is presented in Figs. 4–6, and these results indicate that option 3, namely, the running length $s$ from the stagnation point on the conical portion, gives results that are in close agreement with the DSMC results in all of the cases considered. Except for the conical portion in Fig. 5, where the differences between the two approaches are 20–25%, the agreement between the present results and the DSMC results is excellent. The small difference in the result at the stagnation point in Fig. 5 may be attributed due to the use of radial weighting factor

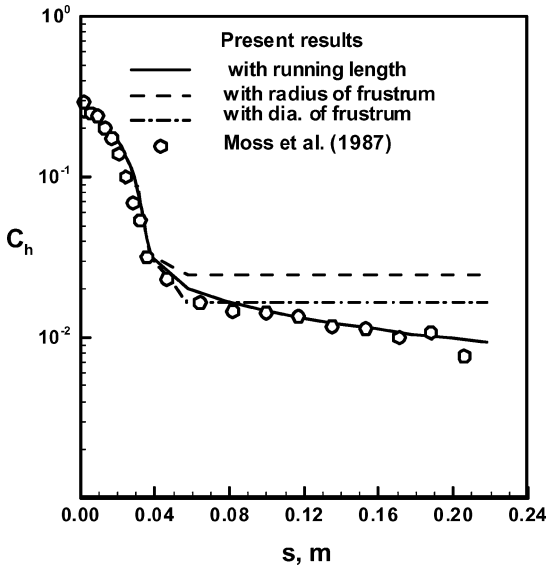


**Fig. 4 Comparison of present results of $C_h$ distributions vs arc length $s$ on a 5-deg sphere–cone at 70-km shuttle flight conditions with Moss et al.[24] results.**

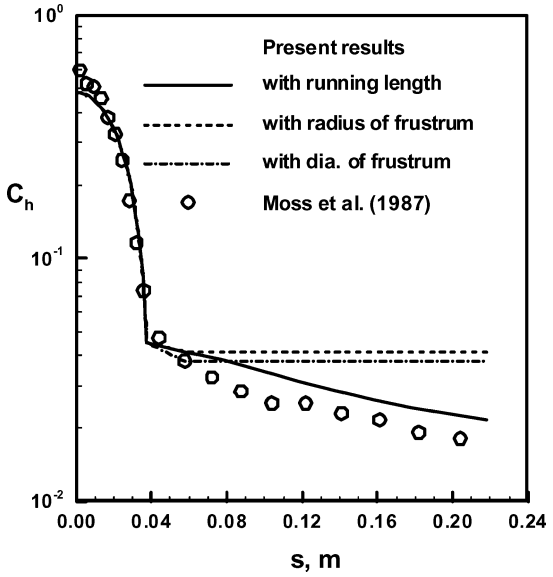


**Fig. 5 Comparison of present results of $C_h$ distributions vs arc length $s$ on a 5-deg sphere–cone at 80-km shuttle flight conditions with Moss et al.[24] results.**

employed in the DSMC simulations. However, the differences of the results on conical portion in Fig. 5 are not understood at the present time.

**Elliptic Paraboloids**

Elliptic paraboloids provide a case to test the capability of the HATLAP method to include three-dimensional effects arising due to crossflow velocity. Unlike the Cooke analogy,[8] there is no restriction on the magnitude of the crossflow velocity in the HATLAP method so long as flow separation does not occur. The validity of the results on elliptic paraboloids of different aspect ratios from the HATLAP method can be established by comparing them with the corresponding three-dimensional VSL solutions with surface and shock slip conditions, as obtained by Tirskii et al.[3] The current approach may prove useful in predicting the aerodynamics and heat fluxes on the windward side of shuttlelike space vehicles by approximating the transverse planes of the windward side with elliptic paraboloids of different aspect ratios.

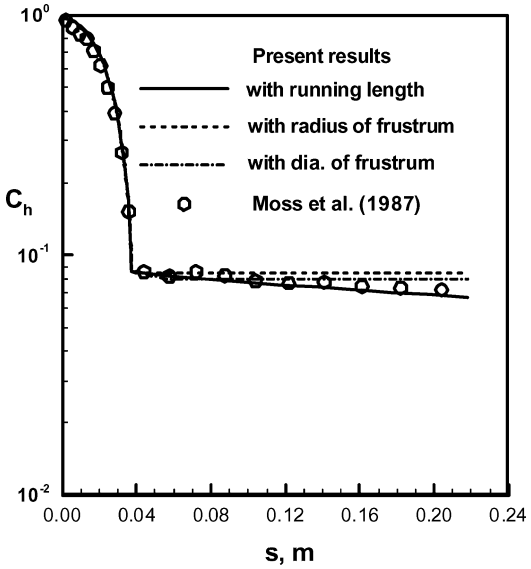


**Fig. 6 Comparison of present results of $C_h$ distributions vs arc length $s$ on 5-deg sphere–cone at 100-km shuttle flight conditions with Moss et al.[24] results.**

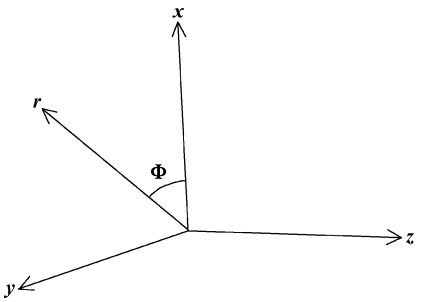


**Fig. 7 Cartesian $(x, y, z)$ and cylindrical $(r, \Phi, z)$ coordinates for elliptic paraboloid.**

The Cartesian equation of an elliptic paraboloid is

$$z = \tfrac{1}{2}(x^2 + ky^2), \qquad k = a^2/b^2 \tag{21}$$

where $z$ is the axis of the elliptic paraboloid and the $y$ axis is perpendicular to the $xz$ plane (Fig. 7), and $a$ and $b$ are related to semiminor and semimajor axes, respectively. Let $\Phi$ be the azimuthal angle that a meridional plane passing through the $z$ axis makes with the $xz$ plane. Cartesian coordinates $(x, y, z)$ and cylindrical coordinates $(r, \Phi, z)$ are shown in Fig. 7. The intersection of a meridional plane with azimuthal angle $\Phi$ is a paraboloid. Cross sections of the elliptic paraboloid with $k = 0.4$ by the meridional planes $\Phi = 0$, 45, 63.4, and 90 deg in the first quadrant of the Cartesian space, are shown in Fig 8. A meridional curve at $\Phi = \Phi^*$ in Fig. 8 indicates the variation of the radial coordinate $r$ from the axis of the elliptic paraboloid, namely, the $z$ axis. The intersection of a plane $z =$ constant with the elliptic paraboloid is an ellipse with semiaxes $\sqrt{(2z)}$ and $\sqrt{(2z/k)}$, lying in the $xz$ and $yz$ planes, respectively. If $z$ continues to increase, the elliptic cross section also increases such that the ratio $a/b = \sqrt{k}$ remains constant. If $k < 1.0$, the distance of any point on the paraboloid from the $z$ axis, that is, the value of the cylindrical coordinate $r$ for a fixed value of $z$, increases from $\sqrt{(2z)}$ (minor axis of the elliptic section) to $\sqrt{(2z/k)}$ (major axis of the elliptic section) as the azimuthal angle $\Phi$ increases from $\Phi = 0.0$ deg in the $xz$ plane to $\Phi = 90$ deg in the $yz$ plane. Hence, the semiminor and semimajor axes of the elliptic cross section for a given value of $z$ are $\sqrt{(2z)}$ at $\Phi = 0$ deg and $\sqrt{(2z/k)}$ at $\Phi = 90$ deg, respectively.

The mean curvature at any point on the elliptic paraboloid along a meridional plane $\Phi$ in cylindrical polar coordinates is given by

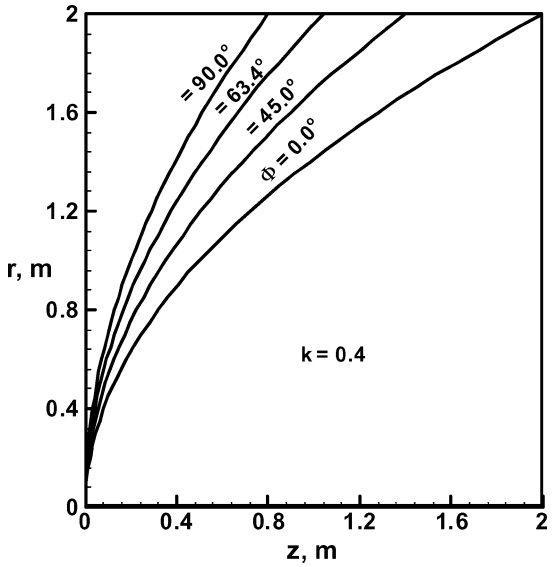


**Fig. 8 Cross sections of elliptic paraboloid with $k = 0.4$ by various meridional planes in the first quadrant of Cartesian space.**

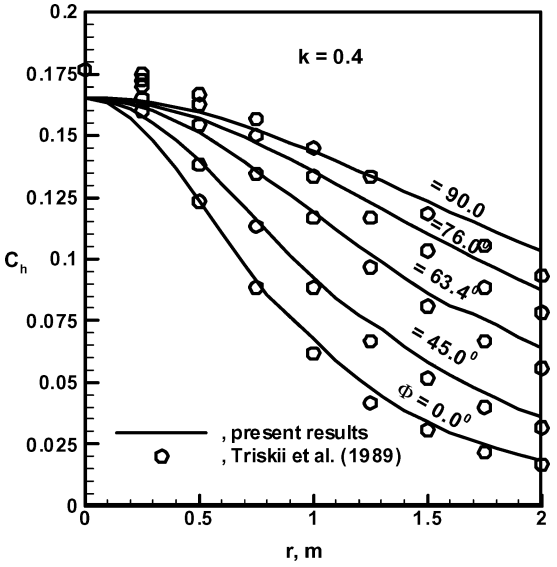


**Fig. 9 Comparison of present results of $C_h$ distribution on various elliptic paraboloid meridional curves with corresponding three-dimensional VSL calculations of Tirskii et al.[3]**

Jain[14] as follows:

$$H = \frac{(1+k) + kr^2(\cos^2\Phi + k\sin^2\Phi)}{2[1 + r^2(\cos^2\Phi + k^2\sin^2\Phi)]^{\frac{3}{2}}} \tag{22}$$

At the stagnation point, $r = 0.0$,

$$H = (1+k)/2 \tag{23}$$

and from Eq. (15),

$$Re_0 = 2/(1+k) \times Re_{01} = \rho_\infty u_\infty/\mu(T_{e0}) \times 2/(1+k) \tag{24}$$

If $k < 1.0$, ($a < b$), then $Re_0$ at a stagnation point of the elliptic paraboloid is greater than the stagnation point of sphere of unit radius ($a = b$ or $k = 1.0$). Following Eq. (10), $C_h$ at the stagnation point of the elliptical paraboloid with $k < 1.0$ is less than that of the spherical stagnation point of unit radius with $k = 1.0$ or $a = b$. This is mainly due to the bluntness effects as explained subsequently. Equation (24) shows that the characteristic length associated with the elliptic paraboloid stagnation point is related to the spherical stagnation point of unit radius with $k = 1$ or $a = b$ by the relation

$$L = [2/(1+k)](1) \tag{25}$$

Equation (25) shows that the flow approaching the stagnation point of the elliptic paraboloid is equivalent to the flow at the stagnation point of a sphere of radius $2/(1+k)$, which is greater than unity. Hence, the shock on the three-dimensional stagnation point or on the equivalent sphere of radius $2/(1+k)$ with $k < 1$ will have greater shock standoff distance, greater boundary-layer thickness, smaller wall temperature gradient, and consequently small heat fluxes in comparison to the corresponding quantities on a sphere of unit radius $k = 1.0$ or $a = b$. Thus, the equivalent sphere of radius $2/(1+k)$ represents the bluntness effect arising due to the three-dimensional nature of the flow at the elliptic paraboloid stagnation point. The bluntness effects result in smaller heat fluxes.

Following Tirskii et al.,[3] the departure of actual pressure on the elliptic paraboloid from the modified Newtonian pressure is accounted by the following expression for $\lambda_1$:

$$\lambda_1 = 1.0 + \frac{4}{15} \times \frac{r^2(\cos^2\Phi + k^3\sin^2\Phi)}{[1 + r^2(\cos^2\Phi + k^2\sin^2\Phi)]^{\frac{3}{4}} \times H(r, \Phi, z)} \tag{26}$$

Hence the characteristic length $L$ in the definition of the stagnation Reynolds number used in Eqs. (1–3) is

$$L = \lambda_1/H \times Re_{01} \tag{27}$$

In Fig. 9, comparison of heat transfer coefficient distributions from the present results in the meridional planes of $\Phi = 0.0$, 45.0, 63.4, 76.0, and 90.0 deg of the elliptic paraboloid of aspect ratio $k = 0.4$ has been made with the corresponding three-dimensional VSL results of Tirskii et al.,[3] under the following prescribed conditions:

$$M_\infty = 10.0, \qquad Re_0 = 100.0, \qquad \gamma = 1.4$$

$$t_{w0} = 0.05, \qquad Pr = 0.71, \qquad \mu \propto \sqrt{T}$$

Here, Reynolds number $Re_0$ is defined with the smaller of the two principal radii of curvatures at the point under consideration on the elliptic paraboloid under consideration. Figure 9 shows that the values of $C_h$ along the meridional plan $\Phi = 0.0$ deg are minimum and values of $C_h$ along meridional plan $\Phi = 90$ deg are maximum. For angles lying between $\Phi = 0.0$ and 90 deg, $C_h$ values along the meridional planes lie between the values of $C_h$ at $\Phi = 0.0$ and 90 deg.

Figure 9 shows that the greatest difference between the present results and the three-dimensional VSL results by Tirskii et al.[3] is about 7% at the stagnation point. Downstream of the stagnation point, the absolute difference between the two results decreases sharply, but due to the small magnitude of the values of $C_h$ involved, the percentage difference still remains almost the same. Note that there is point of inflexion in the curves for $\Phi = 0.0$, 45.0, and 63.4 deg. The reasons for the inflexion points are not clear to the authors. There is no inflexion point in the curves for $\Phi = 76.0$ and 90.0 deg.

Figures 10 and 11 show the pressure and skin-friction coefficient distributions along the meridional planes $\Phi = 0.0$, 45.0, 63.4, 76.0, and 90.0 deg of the elliptic paraboloid with $k = 0.4$. Tirskii et al.[3] did not compute values of $C_p$ and $C_f$ variations along the meridional plane from the three-dimensional VSL solutions. It is not possible to assess the accuracy of the predictions of $C_p$ and $C_f$ variations from the present calculation. Figure 10 shows that the pressure coefficient variations increase smoothly from it minimum values at $\Phi = 0$ deg to the maximum values at $\Phi = 90.0$ deg. There are no points of inflexion in the pressure coefficient variations. Figure 11 shows that, as the axial distance $z$ increases, along a meridional plane, the skin-friction coefficient $C_f$ first increase from its value

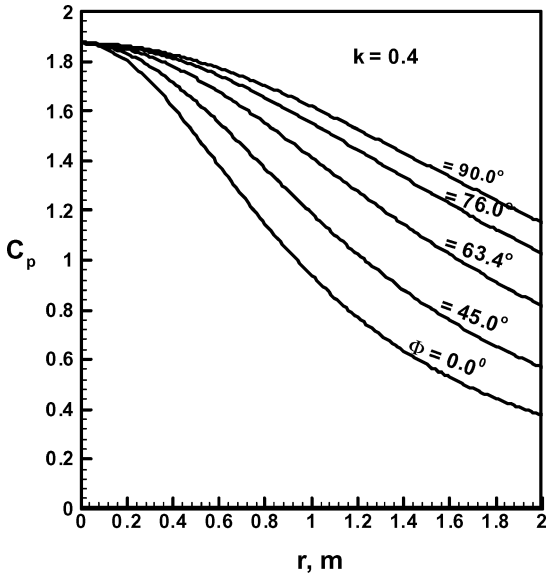


**Fig. 10 Present calculations of $C_p$ distribution on various elliptic paraboloid meridional curves.**

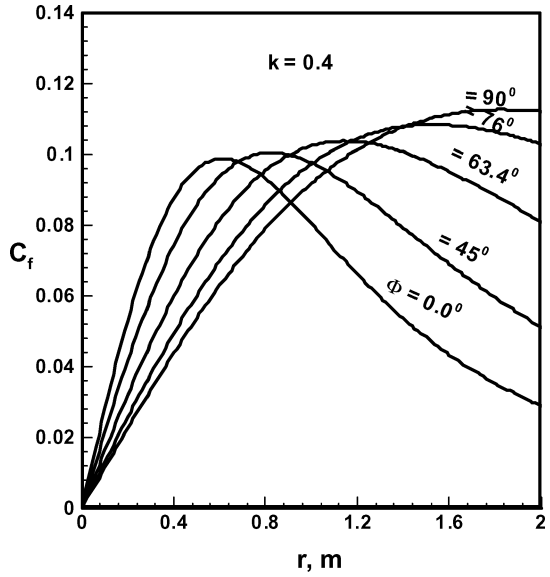


**Fig. 11 Present results of $C_f$ distribution on various elliptic paraboloid meridional curves.**

zero at the stagnation point up to a maximum value and then decreases. The maximum values continue to increase and shift away from the stagnation point as the meridional angle $\Phi$ increases from 0.0 to 90.0 deg. The pattern of $C_f$ variations along any meridional plane is similar to the $C_f$ variation on a blunt-nosed body such as the forepart of a sphere.

In Fig. 12, comparison of heat transfer coefficient distributions for $\gamma = 1.2, 1.4$, and 1.667 at $\Phi = 45.0$ deg meridional plane of the elliptic paraboloid with $k = 0.4$ is made with the corresponding results of Tirskii.[3] It is found that as gamma decreases, wall heat flux increases. Using the Navier–Stokes (NS) method of Jain and Adimurthy,[25,26] Jain and Singh ("On the Stagnation Point Hypersonic Merged Layer Flow," unpublished paper) computed the stagnation point equations through the shock wave with surface slip conditions for different values of gamma under the shuttle flight conditions at 104.93-km altitude. Jain and Singh showed (Fig. 13) that as gamma decreased due to the mixture of several inert gases, VSL thickness decreased, temperature in the VSL decreased, and maximum temperature in the VSL shifted toward the wall, which gave rise to higher wall temperature gradient and higher heat fluxes.

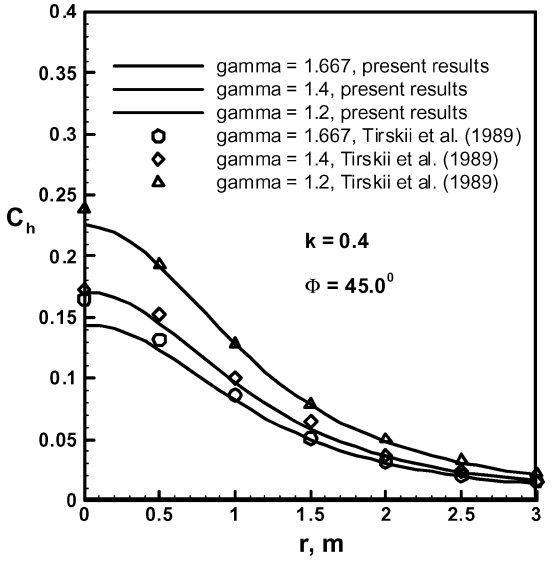


**Fig. 12 Comparison of present results of $C_h$ distribution on elliptic paraboloid with $k = 0.4$ and $\Phi = 45$ deg with the three-dimensional VSL calculations of Tirskii et al.[3]**

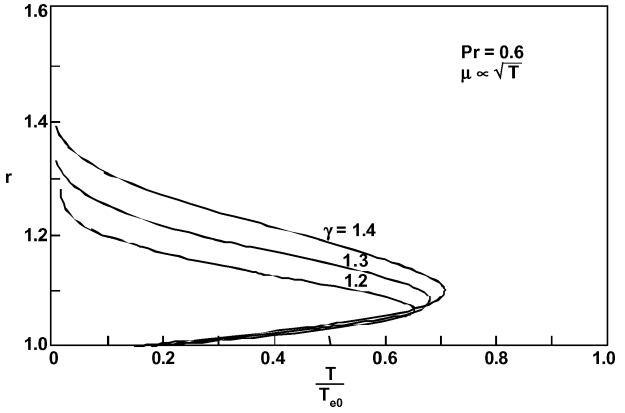


**Fig. 13 NS stagnation point temperature profiles for different values of gamma by Jain and Singh ("On the Stagnation Point Hypersonic Merged Layer Flow," unpublished paper) at 104.93-km shuttle flight conditions.**

The decrease in temperature with a decrease in gamma may be attributed that, as gamma decreases, $C_v$, specific heat at constant volume, increases much faster than the increment in $C_p$, specific heat at constant pressure. The internal energy per unit mass, $e = C_v T$, increases for a unit rise of temperature. Hence, for a given prescribed condition, temperature decreases for a mixture of an inert gas as the value of effective gamma decreases. It is found by Jain and Singh that the effect of changes in gamma on the fluid flow of a mixture of inert gases is realized more in a rarefied medium than in a continuum medium. Changes in effective gamma arising due to changes in the composition of the gas due to chemical reactions may have a different effect on the fluid flow and on the surface quantities. This is because chemical reactions either absorb or generate chemical energy. Thus, the physics of a chemically reacting flowfield is different from that of an inert gas mixture flowfield. In Fig. 12, the percentage difference between the present results and the three-dimensional VSL results of Tirskii et al.[3] at the stagnation point is 13% for $\gamma = 1.667$, less than 1% for $\gamma = 1.4$, and less than 12% for $\gamma = 1.2$. Downstream of the stagnation point, the percentage difference between the two results decreases sharply. Note that the present method gives reasonably accurate results for $C_h$ distribution for different gas composition.

Figure 14 shows that the present results of heat transfer distributions on an elliptic paraboloid with $k = 0.25$ along with the corresponding results of Tirskii et al.[3] under the following high Reynolds

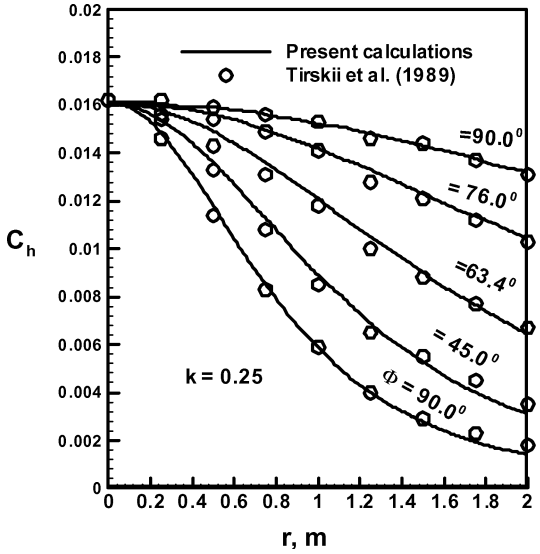


**Fig. 14 Comparison of present results of $C_h$ variations on various elliptic paraboloid meridional curves with $k = 0.25$ with corresponding results of Tirskii et al.[3]**

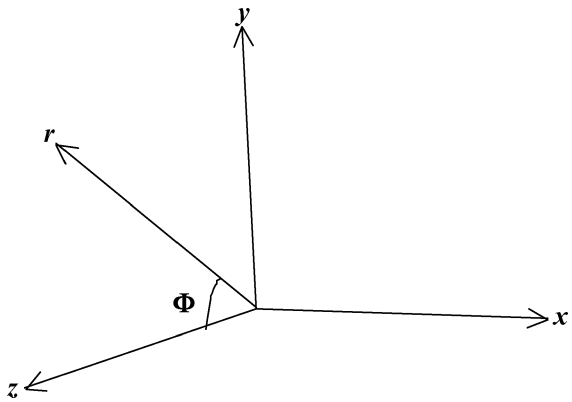


**Fig. 15 Cartesian $(x, y, z)$ and cylindrical $(r, \Phi, x)$ coordinate systems for AFE.**

number conditions in the meridional planes of $\Phi = 0.0$, 45.0, 63.4, 76.0, and 90.0 deg:

$$M_\infty = 5.0, \qquad Re_0 = 10 \times 10^4, \qquad \gamma = 1.4$$

$$t_{w0} = 0.1, \qquad Pr = 0.71, \qquad \mu \propto \sqrt{T}$$

Agreement of the present results with the three-dimensional VSL results of Tirskii et al.[3] is within a few percentage points along each of the meridional planes of the elliptic paraboloid. Note that the present results and Tirskii et al.[3] results agree perfectly at the stagnation point of the elliptic paraboloid.

### AFE Vehicle

The AFE vehicle was designed to reduce drag in the transitional regime and thus save retrorocket fuel. AFE is a vehicle of complex configuration, essentially consisting of three segments. It consists of an ellipsoidal nose, followed by an elliptic cone (raked by a plane inclined at an angle of 73 deg with its axis), and a toroidal skirt tangential to each meridional plane on the elliptic cone. A full description of the AFE geometry is given by Cheatwood et al.[27] An easily comprehensible description of the AFE is presented by Jain.[15] Cartesian coordinate $(x, y, z)$ and cylindrical coordinate $(r, \Phi, x)$ systems for the AFE are shown in Fig. 15. A configuration of the AFE and meridian curves for $\Phi = \pm 90, \pm 60, \pm 40, \pm 20$, and 0.0 deg are shown in Fig. 16. Note that the AFE is a bluff-nosed vehicle with contours of cross sections continuously changing in shape and size as the axial distance from the vertex of the nose increases from the elliptic cone to the toroidal skirt. For such unsymmetric configurations, the characteristic length as derived in Eq. (18) is the following:

$$L = \tilde{H}(x, y, z)/H(x, y, z) \times \lambda/\tilde{H}(0, 0, 0) \tag{28}$$

Analytical expressions for $H(x, y, z)$, $\tilde{H}(x, y, z)$, and $\lambda(x, y, z)$ for various sections of the AFE are given by Jain[15]:

$$Re_0 = L \times Re_{01} \tag{29}$$

The values of Reynolds number $Re_0$ are substituted in Eqs. (1–3) to derive the aerodynamic and thermal load distributions in various meridional planes of the AFE. This procedure reduces the calculations on the complicated three-dimensional configuration to the calculations on an equivalent two-dimensional configuration.

In Table 2, flight conditions of the AFE at the beginning of quiescent period at 80-km altitude and at the peak heating time (76-km altitude) are presented.

The mean curvatures $\tilde{H}(x, y, z)$ and $H(x, y, z)$ represent the axisymmetric and bluntness effects, respectively, and tend to move heat fluxes in opposite directions. Figure 17 shows that in the meridional planes $\Phi = \pm 90$ deg, $\tilde{H}(x, y, z) > H(x, y, z)$, and the axisymmetric effects dominate the bluntness effects. Hence, Fig. 18 shows that the heat flux distribution on the EAB is higher than the heat flux distribution on the AFE for the perfect and the equilibrium gases in the meridional planes $\Phi = \pm 90$ deg. The discontinuities in curvatures at the junctions of ellipsoid and elliptic cone and at elliptic cone and toroidal skirt in Fig. 18 are spurious in nature and should be ignored. Similar discontinuities are evident in heat transfer distributions in Fig. 19 and as subsequently shown. For design purpose, these sharp discontinuities can be replaced by smooth curves. Figure 19 shows that, in the meridional plane $\Phi = 0.0$ deg, $\tilde{H}(x, y, z) < H(x, y, z)$,

**Table 2 Flight conditions of the AFE at 80- and 76-km altitudes**

| Flight condition | 80 km | 76 km |
|---|---|---|
| Velocity $u_\infty$, km/s | 9.715 | 9.306 |
| Temperature $T_\infty$, K | 196.8 | 198.9 |
| Pressure $p_\infty$, N/m$^2$ | 1.227 | 2.134 |
| Wall temperature $T_{\text{wall}}$, K | 1756.0 | 1782.0 |
| Ratio of specific heats $\gamma$ | 1.4015 | 1.4015 |

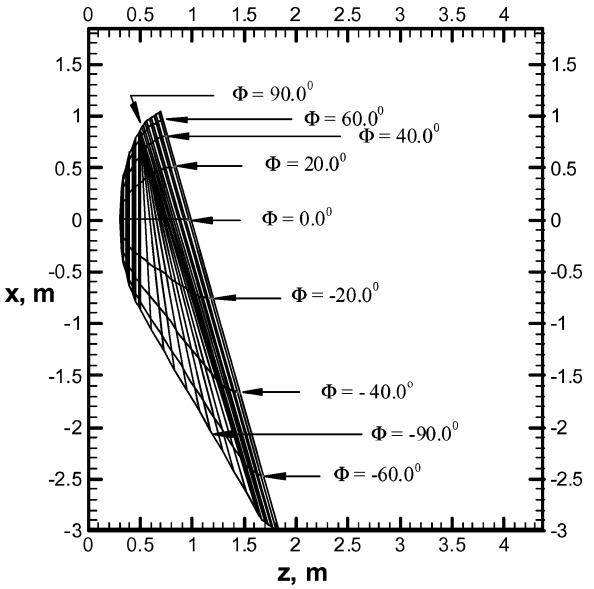


**Fig. 16 Configuration of the AFE and meridian curves for $\Phi = \pm 90$, $\pm 60$, $\pm 40$, $\pm 20$, and 0.0 deg.**

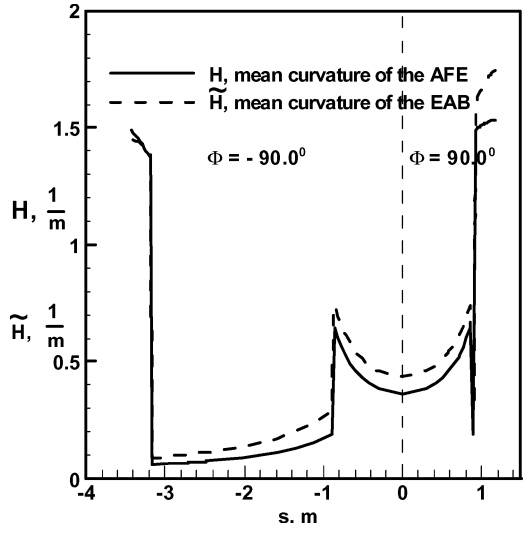


**Fig. 17 Variation of mean curvatures $H(x, y, x)$ and $\tilde{H}(x, y, z)$ vs arc length $s$ on of the AFE and the EAB at $\Phi = \pm 90$ deg.**

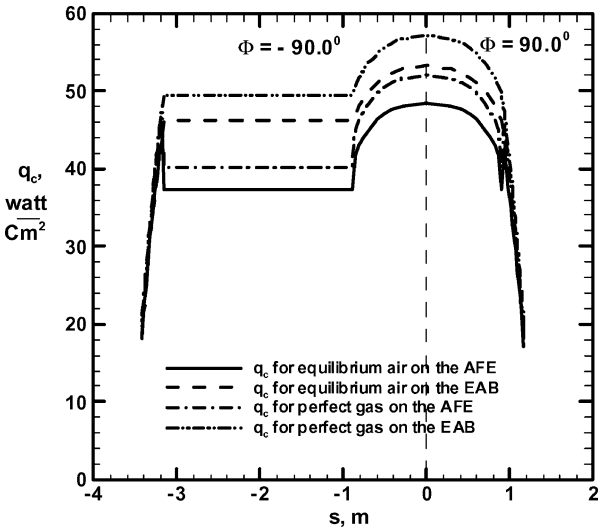


**Fig. 18 Distribution of heat fluxes $q_c$ vs arc length s on the AFE and the EAB at $\Phi = \pm 90$ deg.**

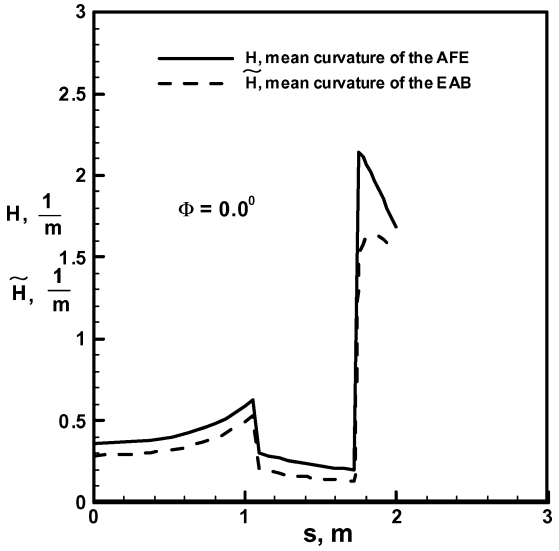


**Fig. 19 Variation of mean curvatures $H(x, y, z)$ and $\tilde{H}(x, y, z)$ vs arc length $s$ on AFE and EAB at $\Phi = 0.0$ deg against arc length $s$.**

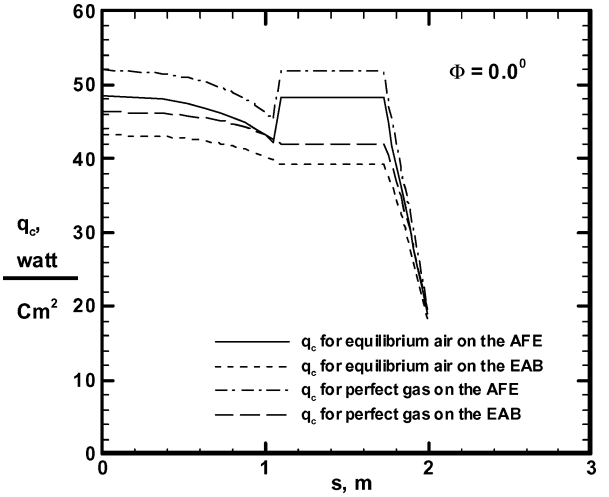


**Fig. 20 Distribution of heat fluxes $q_c$ vs the arc length $s$ on AFE and EAB at $\Phi = 0.0$ deg.**

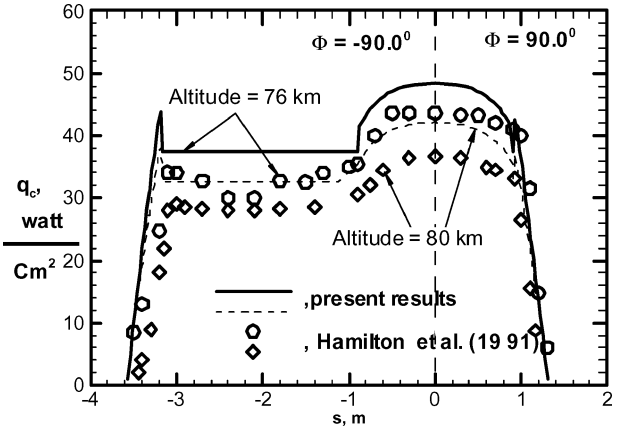


**Fig. 21 Comparison of AFE equilibrium gas heat flux distribution vs arc length $s$ in meridional planes $\Phi = \pm 90$ deg from present calculations with the results of Hamilton and Greendyke.[28]**

indicating the predominance of the bluntness effects over the axisymmetric effects. Figure 20 shows that the heat flux distribution on the AFE is higher than the heat flux distribution on the EAB, both for the perfect and the equilibrium gases in the meridional plane $\Phi = 0.0$ deg. It is found that the changeover takes place in the meridional plane $\Phi = \pm 40$ deg, where $[\tilde{H}(x, y, z)/H(x, y, z)] \approx 1.0$ and heat fluxes on the EAB and the AFE are almost equal. Further note that the heat transfer for the perfect gas is always greater than the heat transfer for the equilibrium gas. This practical example shows that it is difficult to draw any general conclusions about the three-dimensional effects of a general three-dimensional geometry of the body, on heat fluxes.

Hamilton and Greendyke[28] computed heat flux distributions in the meridional planes $\Phi = \pm 90$, $\pm 60$, $\pm 40$, $\pm 20$, and 0 deg of the AFE, for 80 (beginning of quiescent period ) and 76-km (peak heating time) flight conditions, of the AFE entry trajectory. Using a thermochemical nonequilibrium, 11-species, and 2-temperature gas model, they computed the flowfield and heat fluxes on the AFE by using the LAURA code with thin-layer NS approximations. Figures 21–24 present the results from the HATLAP method for equilibrium gas heat flux distributions along the meridional planes $\Phi = \pm 90$, $\pm 60$, $\pm 20$, and 0 deg, of the AFE for both the 80- and 76-km flight conditions. The current results are compared with the corresponding results of Hamilton and Greendyke.[28] Notice that there are kinks in the heat fluxes at the ellipsoid and the elliptic cone junction and at the elliptic cone and circular skirt junction. These kinks in heat fluxes do not have any physical significance, and they arise due to curvature discontinuities on either side of the

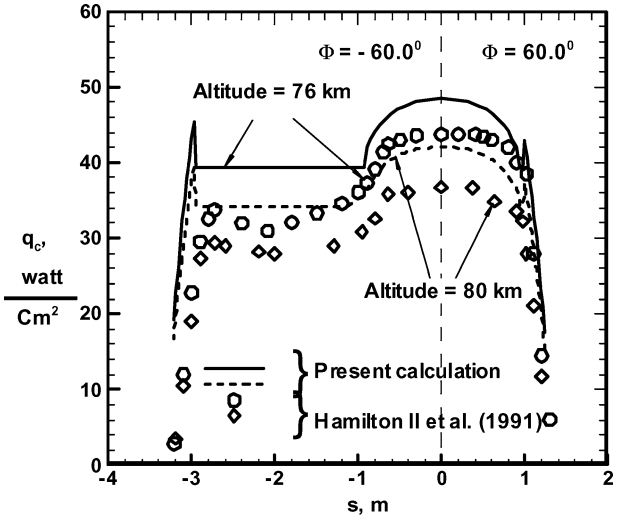


**Fig. 22 Comparison of AFE equilibrium gas heat flux distributions vs arc length $s$ in meridional planes $\Phi = \pm 60$ deg from present calculations with results of Hamilton and Greendyke.[28]**

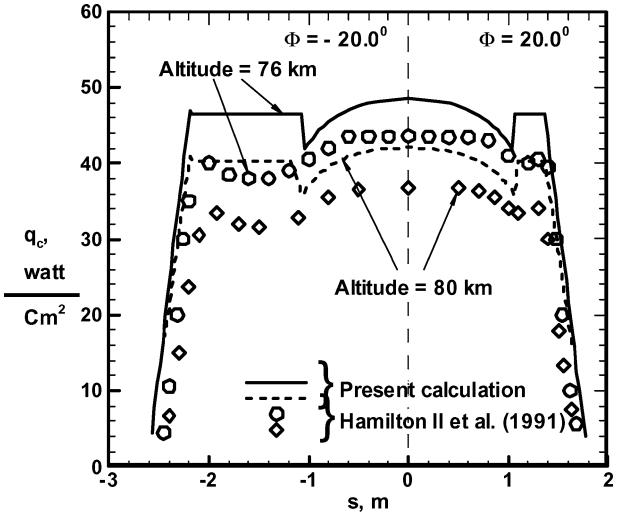


**Fig. 23 Comparison of AFE equilibrium heat flux distribution in meridional planes $\Phi = \pm 20$ deg from present calculations with CFD results of Hamilton and Greendyke.[28]**

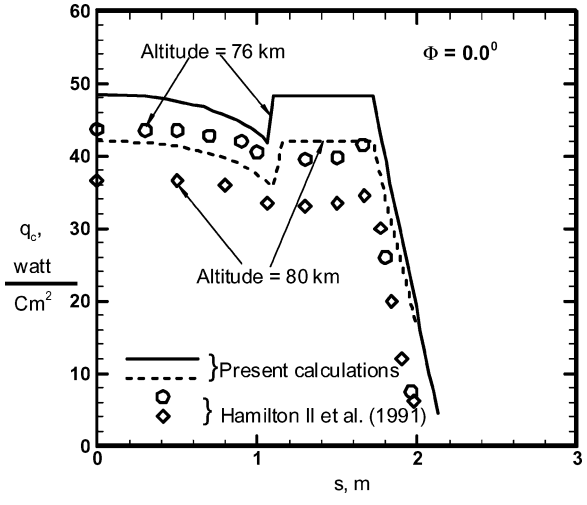


**Fig. 24 Comparison of AFE equilibrium gas heat flux distribution vs arc length $s$ in meridional plane $\Phi = 0.0$ deg from present calculations with results of Hamilton and Greendyke.[28]**

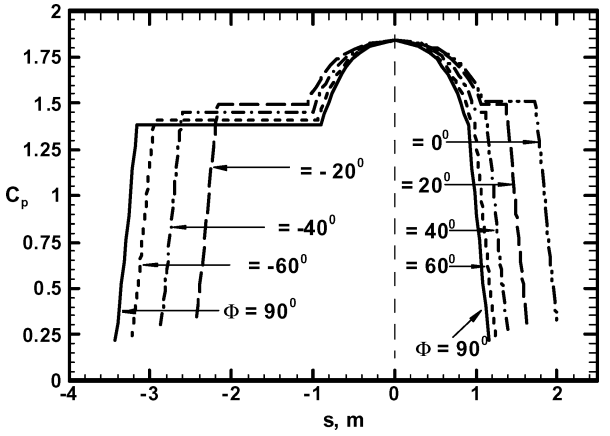


**Fig. 25 Pressure coefficient distributions vs arc length $s$ on the AFE in meridional planes $\Phi = \pm 90$, $\pm 60$, $\pm 20$, and $\pm 0.0$ deg from present calculations.**

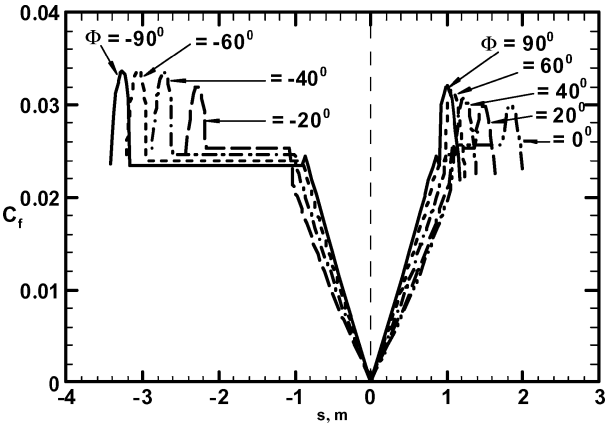


**Fig. 26 Skin-friction coefficient distributions vs arc length $s$ in meridional planes $\Phi = \pm 90$, $\pm 60$, $\pm 20$, and 0.0 deg from the present calculations.**

junctions. These kinks can be removed by the use of smoothing functions.

Figure 21 indicates that good agreement of the current results with the CFD results exist on the ellipsoidal nose and on the short arm of the AFE for $\Phi = \pm 90$ deg. Under the peak heating conditions (76 km), the difference between the present calculations and the CFD results varies from 10% at the stagnation point to 5% at the far end of the ellipsoidal nose. Because of nonequilibrium dissociation and recombination in the expansion zone over the elliptic cone, the LAURA code probably computes a net release of energy that overexpands the flow after each junction and causes the heat flux to dip down much more than is expected under equilibrium conditions. The maximum difference between the present calculations and the CFD results of Hamilton and Greendyke[28] is 18%. Similar agreement of the results from the HATLAP method with the CFD results have been obtained for the meridional planes $\Phi = \pm 60$, $\pm 20$, and 0 deg shown in Figs. 22, 23, and 24, respectively.

The present results give almost constant values of heat fluxes over the long elliptic arm of the AFE. Using three-dimensional explicit NS equations with thermochemical nonequilibrium and 11-species gas model, Palmer[29] computed the heat fluxes in the meridional planes $\Phi = \pm 90$ deg of the AFE under 77.8-km flight conditions. Because the flight conditions in the Palmer[27] computations are different from those used in our calculations, it is difficult to compare the results quantitatively, but it is important to notice that the variation of heat fluxes on the long elliptic arm in the meridional plane of $\Phi = -90$ deg is almost constant, similar in nature to the results obtained in the present calculations from the HATLAP method.

For the sake of completeness, pressure and skin-friction distributions in the AFE meridional planes of $\Phi = \pm 90$, $\pm 60$, $\pm 40$, $\pm 20$,

and 0 deg are shown in Figs. 25 and 26 for 76-km AFE flight conditions. Because the LAURA code does not provide the results of pressure and skin-friction distributions, it is not possible to assess the accuracy of the present calculations.

## Conclusions

A new approach is introduced to predict three-dimensional effects on surface quantities through geometrical quantities associated with the body rather than the fluid mechanics of the body. The present procedure has a wider range of applications in that it has no restrictions on the magnitude of the crossflow velocity. The procedure is valid before fluid separation takes place. The geometrical quantities relevant to the problem must be calculated only once, and the method can then be used for the entire flight trajectory of the vehicle with ease. The validity of the results is established by comparing the results with the available results from more detailed and tedious computations and experimental measurements.

In most cases, either the pressure or the heat fluxes on a three-dimensional body is given. There is need to develop reliable and accurate results for pressure, skin-friction and heat flux distributions on three-dimensional bodies with triaxial axis so that the present code can be tested to predict aerodynamics as well as thermal loads on vehicles in a consistent manner. Additional CFD, DSMC, wind-tunnel, and flight data will enable us to establish clearly the geometry of bodies where different values of characteristic lengths are applicable.

Under hypersonic conditions, the flow in often laminar. However, due to roughness, gaps, or excessive vehicle length, the flow may become turbulent. In the present investigation, effects of turbulence are not considered.

## Acknowledgment

The work was performed under Small Business Innovation Research Phase II, Contract F33615-98-C-3000, from the U.S. Air Force Research Laboratory, Wright–Patterson Air Force Base, Ohio.

## References

[1]Jain, A. C., and Hayes, J. R., "Hypersonic Pressure, Skin-Friction, and Heat Transfer Distributions on Space Vehicles: Planar Bodies," *AIAA Journal*, Vol. 42, No. 10, 2004, pp. 2060–2069.

[2]Weatherburn, C. E., *Differential Geometry of Three Dimensions*, Cambridge Univ. Press, London, 1964, pp. 66–78.

[3]Tirskii, G. A., Brykina, I. G., Rusakov, V. V., and Scherbak, V. G., Inst. of Mechanics, Rept. No. 3815, M. V. Lomonosovs Moscow Univ., Moscow, Nov. 1989.

[4]Fivel, H. J., "Numerical Flow Field Program For Aerodynamic Heating Analysis," *Equations and Results*, Vol. 1, U.S. Air Force Flight Dynamics Lab., Rept. AFFDL-TR-79-3128, Wright–Patterson AFB, OH, Dec. 1979.

[5]Zoby, E. V., and Simmonds, A. L., "Engineering Flowfield Method and Angle-of-Attack Applications," *Journal of Spacecraft and Rockets*, Vol. 22, No. 4, 1985, pp. 398–404.

[6]Engel, C., and Praharaj, S. C., "MINIVER Upgrade for the AVID System," *LANMIN Users Manual*, Vol. 1, NASA CR 172212, Aug. 1983.

[7]Hender, D. R., "A Miniature Version of the JA70 Aerodynamic Computer Program, H800 (MINIVER)," McDouglas Astronautics Co., MDC Rept. G.0462, Huntington Beach, CA, revision Jan. 1972.

[8]Cooke, J. C., "An Axially Symmetric Analogue For General Three-Dimensional Boundary Layers," British Aeronautical Research Council, Rept. and Memorandum No. 3200, London, 1961.

[9]Jain, A. C., "Mathematical Formulation of Predicting Pressure, Skin-Friction, and Heat Flux Distributions on Space Vehicles of Arbitrary Shape," Science and Technology Corp., STC TR 3313, Hampton, VA, March 2003.

[10]Reshotko, E., "Heat Transfer to a General Three-Dimensional Stagnation Point," *Jet Propulsion*, Vol. 28, Jan. 1958, pp. 58, 59.

[11]Fay, J. A., and Riddell, F. R., "Theory of Stagnation Point Heat Transfer in Dissociated Air," *Journal of Aerospace Sciences*, Vol. 25, No. 2, 1958, pp. 73–85.

[12]Lees, L., "Laminar Heat Transfer over Blunt-Nosed Bodies at Hypersonic Flight Speeds," *Jet Propulsion*, Vol. 26, April 1956, pp. 259–269.

[13]Golovachov, Y. P., *Numerical Simulation of Viscous Shock Layer Flows*, Kluwer Academic, London, 1995, pp. 154–247.

[14]Jain, A. C., "Pressure, Skin-Friction and Heat Transfer Distributions on Elliptic Paraboloids at Zero Angle of Attack," Science and Technology Corp., STC TR 3186(9), Hampton, VA, Nov. 2001.

[15]Jain, A. C., "Three-dimensional Effects on Heat Transfer distribution on Space Vehicles of Arbitrary Shape," Science and Technology Corp., STC TR 3186(8), Hampton, VA, Feb. 2001.

[16]Moss, J. N., and Bird, G. A., "Direct Simulation of Transitional Flow for Hypersonic Reentry Conditions," AIAA Paper 84-0223, Jan. 1984.

[17]Gupta, R. N., "Navier–Stokes and Viscous Shock-Layer Solutions for Radiating Hypersonic Flows," AIAA Paper 87-1576, June 1987.

[18]Nicolet, W. E., "Users Manual for the Generalized Radiation Transfer Code (RAD/ EQUIL)," NASA CR-116353, Oct. 1969.

[19]Balakrishnan, A., Park, C., and Green, M. J., "Radiative Viscous Shock Layer Analysis of FIRE, Apollo, and PAET Flight DATA," AIAA Paper 85-1064, June 1985.

[20]Nicolet, W. E., and Balakrishnan, A., "Radiation Shock Layer Environment (RASLE) Users Manual," Acurex Corp./Aerotherm, Rept. UM 79-10/AS, Mountain View, CA, 1979.

[21]Jain, A. C., "Asymmetric/Axisymmetric Stagnation Point Heat Flux on 3-Dimensional Bodies with Equilibrium Chemistry and Radiation," Science and Technology Corp., STC TR 3186(3), Hampton, VA, Dec. 1998.

[22]Neuenschwander, W. E., "Explicit Relationships for the Thermodynamic Properties of Molecular and Dissociated Air Mixtures to 25000 degree R.," AIAA Paper 89-1735, June 1989.

[23]Jain, A. C., and Prabha, S., "A Comparative Study of Stagnation Point Hypersonic Viscous Shock Layer and Hypersonic Merged Layer Flows," *Proceedings of the 14th International Symposium on Rarefied Gas Dynamics*, edited by H. Oguchi, Univ. of Tokyo, Tokyo, 1984, pp. 241–248.

[24]Moss, J. N., Cuda, V., Jr., and Simmonds, A. L., "Nonequilibrium Effects For Hypersonic Transitional Flows," AIAA Paper 87-0404, Jan. 1987.

[25]Jain, A., and Adimurthy, V., "Hypersonic Merged Shock Layers, Part 1: Adiabatic Wall Case," *AIAA Journal*, Vol. 12, No. 3, 1974, pp. 342–347.

[26]Jain, A., and Adimurthy, V., "Hypersonic Merged Shock Layers, Part 2: Cold Wall Case," *AIAA Journal*, Vol. 12, No. 3, 1974, pp. 348–354.

[27]Cheatwood, F. M., DeJarnette, F. R., Hamilton, H. H., II, "General Description for a Proposed Aeroasssist Flight Experiment Vehicle," NASA TM 87714, July 1986.

[28]Hamilton, H. H., II, and Greendyke, R. B., "Calculation of Radiative and Convective Heating on the Forebody Shield of the Aeroassist Flight Experiment Vehicle," NASA TM 104103, May 1991.

[29]Palmer, G., "Enhanced Thermochemical Nonequilibrim Computations of Flow Around Aeroassist Flight Experiment Vehicle," AIAA Paper 90-1702, June 1990.

C. Kaplan
*Associate Editor*